Asymmetric Flowfield Development on a Slender Body at High Incidence

A. B. Wardlaw Jr.* and W. J. Yanta*
Naval Surface Weapons Center, Silver Spring, Maryland

A rigidly supported tangent ogive model has been tested in low-turbulence incompressible flow at an incidence of 45 deg. A constant streamwise Reynolds number of 1.5×10^5 was maintained that produced laminar boundary-layer separation. Both unsteady surface pressures and flowfield velocities in the cross-flow plane were measured, the latter with a two-component laser Doppler velocimeter. For a case featuring high side forces, the flowfield in the vicinity of the leeside of the model surface was examined in detail. Results indicate that two secondary vortex-like structures featuring vorticity of opposite signs form on each side of the model. Cross-flow plane streamlines are determined by integrating measured cross-flow plane velocities. The resulting streamline structure differs significantly from the anticipated three-dimensional streamline behavior. The evolution of the asymmetric flowfield up to the point of maximum side force is described in terms of cross-flow plane topology.

Nomenclature

$\bar{C}_p$ = average value of $(p-p_\infty)/(q\sin^2\alpha)$ for 100 data points taken at each visit to a pressure tap
C_y = $F_y/(Dq\sin^2\alpha)$
$C_{y_{peak}}$ = maximum C_y value
D = model diameter (5.715 cm)
F_y = side force per unit length
q = freestream dynamic pressure
Re_s = Reynolds number based on freestream properties and $D/\sin\alpha$
U_∞ = freestream velocity
v,w = velocity components in y,z directions
x,y,z = Cartesian coordinates (see Fig. 1)
α = angle of attack
Γ = circulation, m^2/s
λ = $\Gamma/(\pi DU_\infty\sin\alpha)$, s^{-1}
ϕ = circumferential angle (windward is $\phi=180$ deg)
σ_{C_p} = standard deviation of C_p
σ_{V_c} = $\sqrt{\sigma_v^2+\sigma_w^2}$, where σ_v and σ_w are the standard deviations of v and w, respectively
Φ = model roll orientation
ω = [Γ/unit area] $D/(\pi U_\infty\sin\alpha)$

I. Introduction

AT incidences greater than a few degrees, the flow on the leeside of a slender configuration separates and rolls up to form a pair of symmetric vortices. With increasing angle of attack, the pattern becomes asymmetric, even on axisymmetric bodies. In subsonic and transonic flow, these vortices have a dominant and nonlinear influence on vehicle aerodynamics.

The asymmetric vortex pattern that develops on a circular body at high angles of attack has been studied extensively.[1-12] In the subsonic regime this flow produces a large side force that has been difficult to repeat experimentally. Even on axisymmetric bodies, the side force varies with changes in the model roll orientation.[13,14] The nonrepeatability appears to be due primarily to the occurrence of a multiplicity of stable vortex patterns. Such patterns have been documented by the authors in Ref. 12. The different patterns are most likely triggered by model irregularities on the order of the machining tolerance that occur in the vicinity of the nose tip. Unsteadiness can also contribute to the lack of repeatability problem. Freestream turbulence causes the vortex pattern to jump from one stable configuration to another.[12,13]

In the present study, cross-flow plane velocities and surface pressures have been measured on sharp and slightly blunted tangent ogive models at an incidence of 45 deg under the condition of laminar separation. This paper is limited to a discussion of results obtained on the sharp model tested with a grit nose tip designed to stabilize the flowfield. A complete report on all the acquired data is provided in Ref. 15.

The model, instrumentation, and testing procedure are described in Sec. II, while the nose tip and its effect are reviewed in Sec. III. The flowfield development is discussed in Secs. IV. and V, and conclusions are summarized in Sec. VI.

II. Description of the Model and Experiment

Experiments were conducted in the Naval Academy 1×1.3 m subsonic tunnel, which has a nominal freestream turbulence level of 0.1%. Tests were restricted to incidences of 45 deg and freestream velocities of 24 m/s, producing an Re_s of 1.5×10^5. As discussed in Ref. 10, this resulted in laminar boundary-layer separation. The model was mounted on the wind-tunnel wall using the support system illustrated in Fig. 1. To increase the rigidness of the mounting, four support wires were attached to the model at a distance of 12.6 calibers from the nose tip.

The experimental model shown in Fig. 1 was a 5.715 cm diameter tangent ogive with a nose fineness of 3 and an afterbody length of 9.6 calibers. Six cross-sectional stations were each instrumented with 24 pressure taps located circumferentially at intervals of 15 deg. Pressures were monitored using three internally mounted ±0.7 kPa (±0.1 psi) Setra differential pressure transducers. Each of these devices was connected to a 48-port internally mounted Scanivalve allowing all 144 pressure taps to be sampled. Pretest calibrations indicated that pressure fluctuations on the order of 500 Hz could be measured.

Cross-flow planes were surveyed using a two-dimensional, two-color laser Doppler velocimeter (LDV) system in the backscatter mode with off-axis collection optics. The wind-tunnel wall opposite to the model was fitted with a 1.27 cm thick glass window from which the cross-flow planes could be viewed. The laser beams from the LDV system passed into the

Presented as Paper 82-0343 at the AIAA 20th Aerospace Sciences Meeting, Orlando, Fla., Jan. 12-14, 1982; received Aug. 30, 1982; revision submitted June 3, 1983.

*Aerospace Engineer. Associate Fellow AIAA.

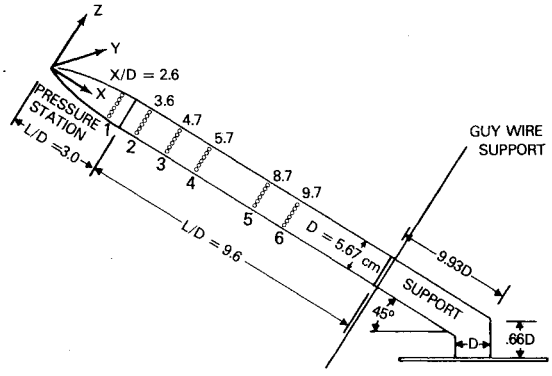

Fig. 1 Tangent ogive pressure model and support.

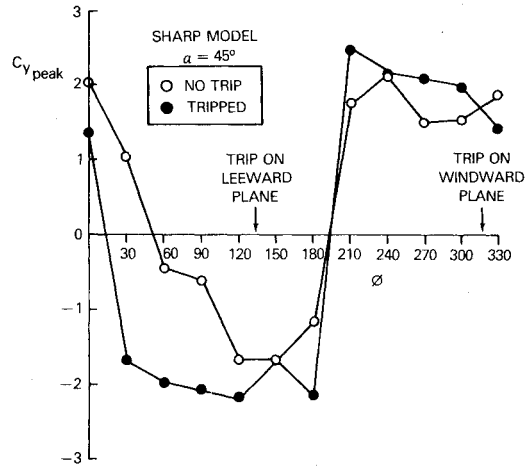

Fig. 2 $C_{y_{peak}}$ as a function of model roll angle.

tunnel through the window. The refraction resulting from the oblique passage of the laser beams through the glass window was accounted for by optically aligning the system inside of the wind tunnel. Brag cell frequency shifting was employed for flow direction determination. The flow was seeded using olive oil particles atomized to a mean diameter of 1.5 μm and a geometric standard deviation of 1.7. Analytic simulations indicated particle lag was not a significant problem.

Pressure-alone tests were initially made at the 12 roll angles: 0, 30, 60,...330 deg. Measurements were integrated to determine the magnitude of the normal and side forces. The model was then positioned to a roll orientation featuring maximum side force and detailed flow surveys were initiated. Cross-flow plane surveys were made at the axial locations of 0.75, 1.3, 2.6, 3.6, and 4.7 calibers.

The surface pressure data were acquired three ports at a time using the internally mounted Scannivalves and transducer arrangement. At each pressure port, 100 samples were taken that allowed both pressure mean and standard deviation values to be determined. The LDV velocity data were measured by focusing the system on a specified point in the flowfield. Velocity measurements were acquired whenever both v and w components were measured within a 100 μs window. Here 100 samples were also taken at each point in the flowfield, allowing both the mean and standard deviation values to be calculated. In the secondary flow region near the leeside of the model surface, measurements were taken with a y, z spacing that varied from 0.76 mm near the model nose tip to 1.27 mm on the afterbody cross-flow planes. Farther from the model surface this spacing was increased by a factor of 3-4. Pressure-alone tests could be completed in about 10 min, while the LDV surveys measuring velocities at as many as 800 points in a cross-flow plane took up to 3 h.

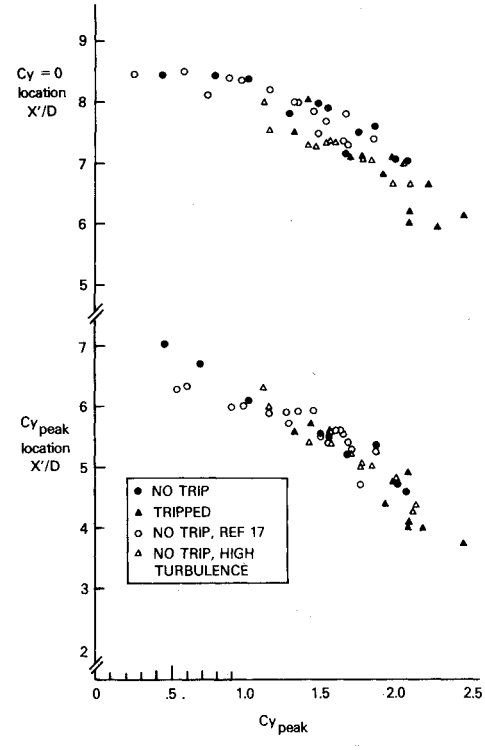

Fig. 3 Axial location of $C_{y_{peak}}$ and $C_y = 0$.

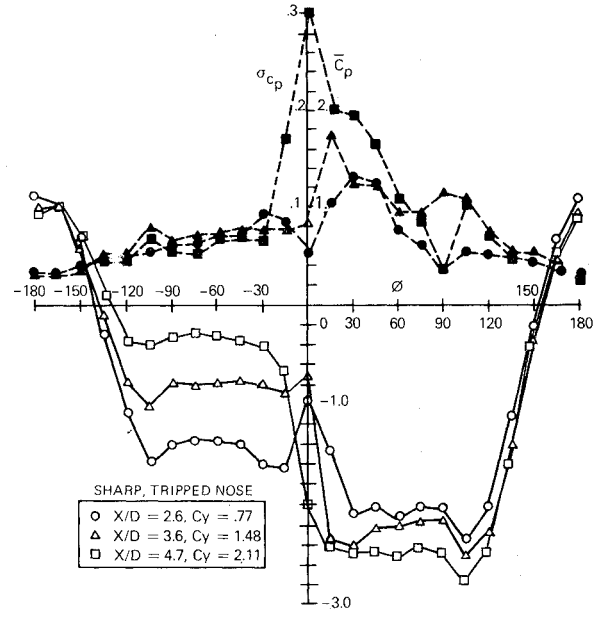

Fig. 4 Circumferential pressure distribution (open symbols are $\bar{C}_p$ and solid ones σ_{C_p}).

III. Influence of the Nose Trip

During the long experiments in which cross-flow plane velocities were measured, the flowfield occasionally changed level of asymmetry. This was determined by monitoring surface pressures throughout the tests. To stabilize the flowfield, a trip made of 0.45 mm grit was added to the model nose in a strip 0.5 cm long and 1 mm wide. The forward edge of the trip was located 2 mm aft of the tip. This type of device has been successfully used by other investigators for this purpose.[16] The magnitude of the peak local side force $C_{y_{peak}}$ with and without the trip in place is illustrated in Fig. 2. The addition of the trip usually increased $C_{y_{peak}}$, particularly at roll orientation featuring low side force levels in the untripped

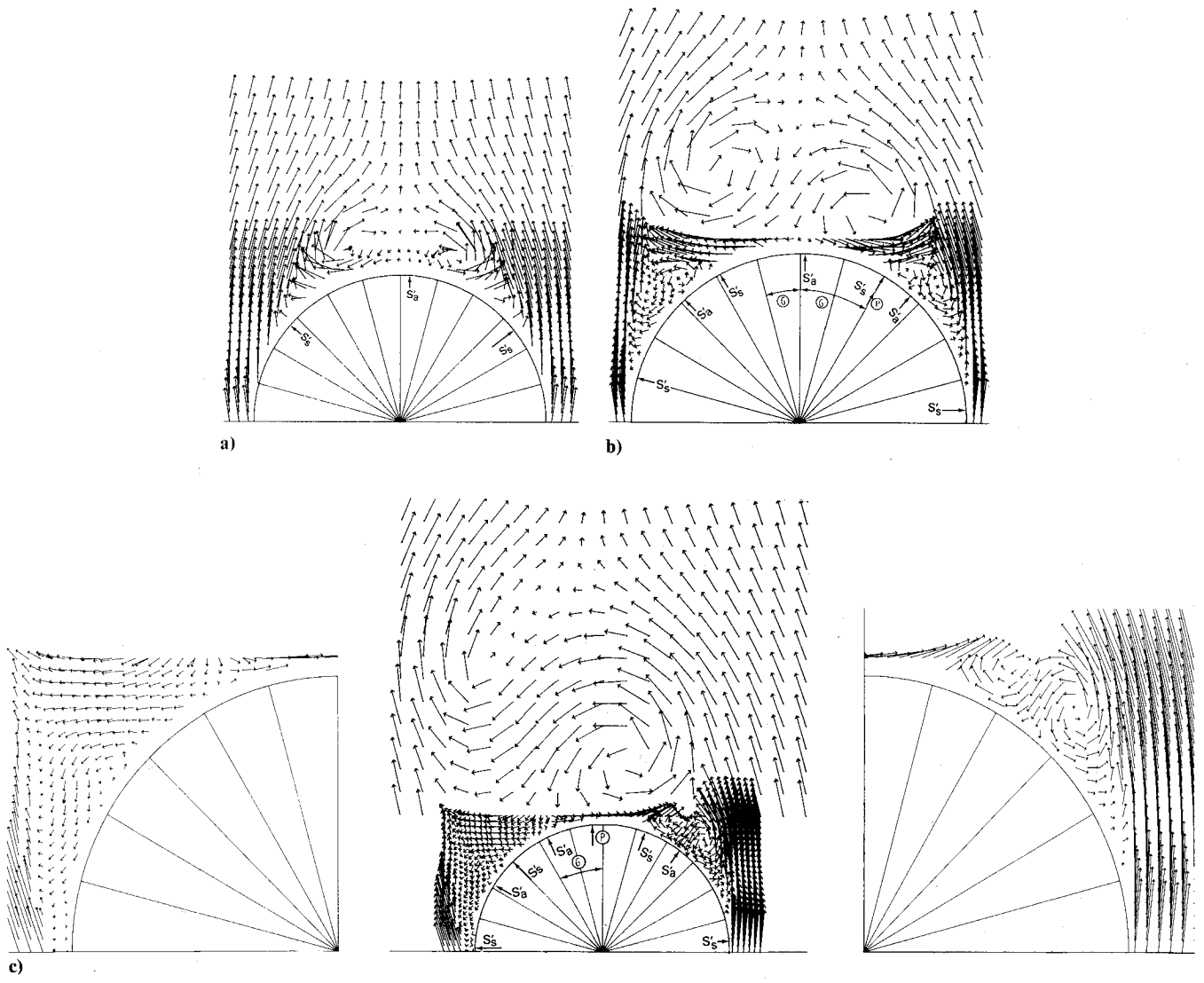

Fig. 5 Measured cross-flow plane velocity vectors (S'_a and S'_s are attachment and separation points, respectively; P represents the peak σ_{C_p} locations while the G indicates regions of sharp pressure gradients).

Table 1 Circulation contained in regions P, S1, and S2

	Left-hand side			Right-hand side				
	Secondary		Primary	Secondary		Primary		
X/D	λ_{s1}	λ_{s2}	λ_p	λ_{s1}	λ_{s2}	λ_p	$\Sigma\lambda$	C_y
0.75			−0.019			0.010	−0.009	
1.30			−0.218			0.198	−0.020	
2.60	−0.218	0.053	−0.403	0.209	−0.046	0.360	−0.044	0.77
3.60	−0.265	0.048	−0.581	0.245	−0.070	0.528	−0.095	1.475
4.70[b]	−0.332[a]	0.031	−0.755	0.297	−0.064	0.665	−0.158	2.1

[a]Estimated. [b]Second vortex with a $\lambda = 0.0023$ starts to form on left-hand side of model.

case. The grit trip also was found to produce a side force that was repeatable throughout long experiments. In successive tests the values of $C_{y_{peak}}$ repeated well; however, some variations were noted in the C_y values measured at stations 1 and 2. Application of a tape trip with a similar planform produced a more drastic effect that included reversal of the side force direction. This is more in keeping with the results of Ref. 16 where a tape trip controlled the side force direction, except at roll orientations that placed the trip near the windward plane.

Although addition of the trip stabilizes the flowfield, it is relevant to ask whether it also alters its fundamental character. It was noted in Ref. 12 that a side force characteristic which appears repeatable from test to test and facility to facility is the relation between the axial location at which $C_{y_{peak}}$ or $C_y = 0$ occur and the magnitude of $C_{y_{peak}}$. If the character of the flowfield is unchanged by the addition of the trip, the tripped data should reproduce the previously observed relationship. As is shown in Fig. 3, data taken on the untripped model from both this study and Ref. 12 are in reasonable agreement with the tripped results. This suggests that the trip locks the flowfield into a pattern typical of the untripped model and does not fundamentally alter its character.

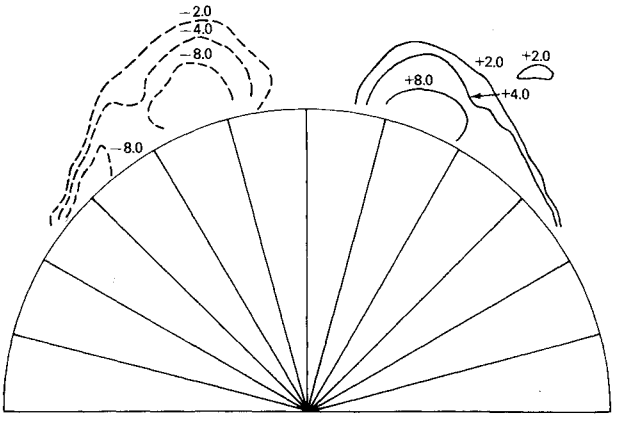

a) $X/D = 1.3$.

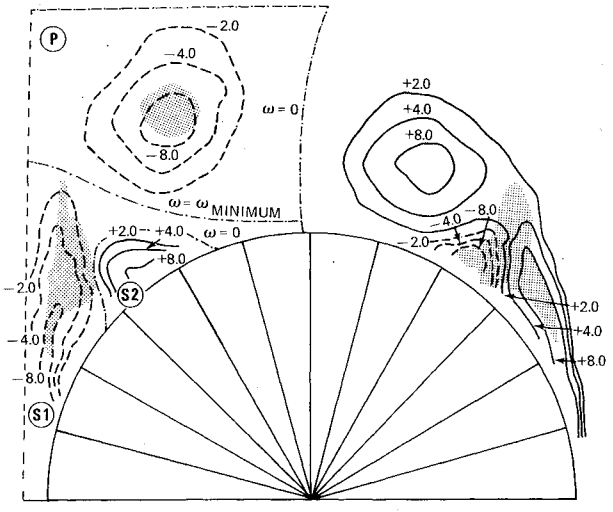

b) $X/D = 2.6$, $C_y = 0.77$.

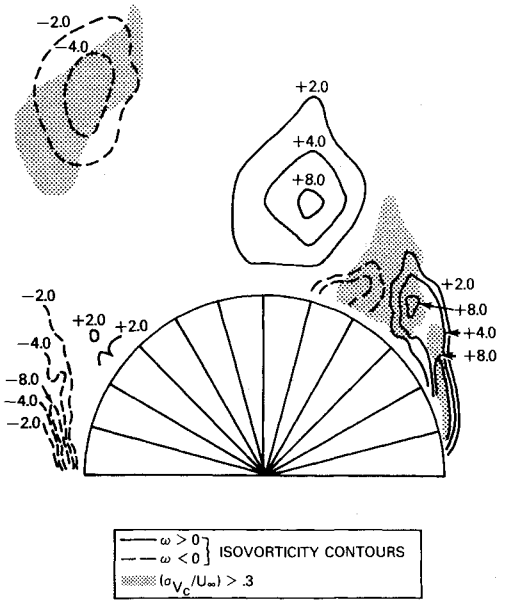

c) $X/D = 4.7$, $C_y = 2.11$.

Fig. 6 Isovorticity contours and area of high-velocity fluctuation.

IV. Flowfield Description

Velocity and Pressure Measurements

Pressure and velocity data taken at a roll orientation featuring a high side force level are shown in Figs. 4 and 5, respectively. Clearly visible are two large, or primary, vortices. In between these vortices there is a saddle or stagnation point that will be referred to as the primary saddle. The secondary region on each side of the model often contains two vortices with opposite rotation and a saddle. In other instances only a single secondary vortex is present in this secondary region. A number of attachment and separation points occur on the model surface. In all cases, an attachment point is visible near the center of the model on the leeside and on each side of the model a separation point can be seen marking the windward extend of the separation region. These attachment and separation points will be referred to as the *rear attachment* and *primary separation* points, respectively. When secondary vortices occur, an additional separation and attachment point occur on each side of the model. In Fig. 5, attachment and separation points are marked by an S_a' and S_s', respectively. The location of the windward separation point on each side of the model is estimated using both velocity and pressure data.

The vorticity throughout the flowfield is calculated by dividing the surveyed portion of the cross-flow plane into quadrilateral elements with the corners located at points where the flowfield velocities are measured. The circulation associated with each element is determined from

$$\Gamma = \oint \bar{v}\ \mathrm{d}\ \bar{\ell} = \tfrac{1}{2}[\bar{n}_{12}\cdot(\bar{v}_1+\bar{v}_2)+\bar{n}_{23}\cdot(\bar{v}_2+\bar{v}_3)$$
$$+\bar{n}_{34}\cdot(\bar{v}_3+\bar{v}_4)+\bar{n}_{41}\cdot(\bar{v}_4+\bar{v}_1)] \quad (1)$$

where $\bar{n}_{ij}$ is the vector connecting element corners i and j while $\bar{v}_i$ is the velocity at corner i. The computed circulation is assigned the location of the element centroid. Isovorticity contours resulting from this calculation are displayed for axial stations with X/D values of 1.3, 2.6, and 4.7 in Fig. 6. Also indicated in this figure are the regions of high-velocity fluctuations.

A convenient method of characterizing the cross-flow plane is to divide it into regions containing vorticity of the same sign. The circulation computed at each element in the cross-flow plane is assigned to one of these regions, allowing the total circulation in each region to be calculated. Elements that do not possess a symmetric counterpart with respect to the pitch planes are excluded from summation. The cross-flow plane is divided into a left and right side. Each side is further decomposed into a primary region P and two secondary regions S1 and S2 containing vorticities of opposite sign. Figure 6 provides a sketch of these regions along with a definition of region boundaries. A listing of the calculated vorticity contained in ecah region is given in Table 1.

The tabulated circulations for the surveyed cross-flow planes are shown in Table 1. On each plane a net negative circulation occurs that increases in magnitude in rough portion to increases in the local side force coefficient. Also indicated in this table are the circulation strengths of the primary and secondary regions P, S1, and S2 associated with each side of the model. As expected, the largest circulation occurs in P followed by that in S1, which is of about half the magnitude. The circulation of region S2 is on the order of a tenth of that in P.

It is important to note that the circulation contained in each region cannot necessarily be associated with a vortex since not all regions contain vortices. Also, in region S1, there often exists both a strong shear layer that springs from the separation point and a vortex. Here the circulation attributable to each structure cannot be determined.

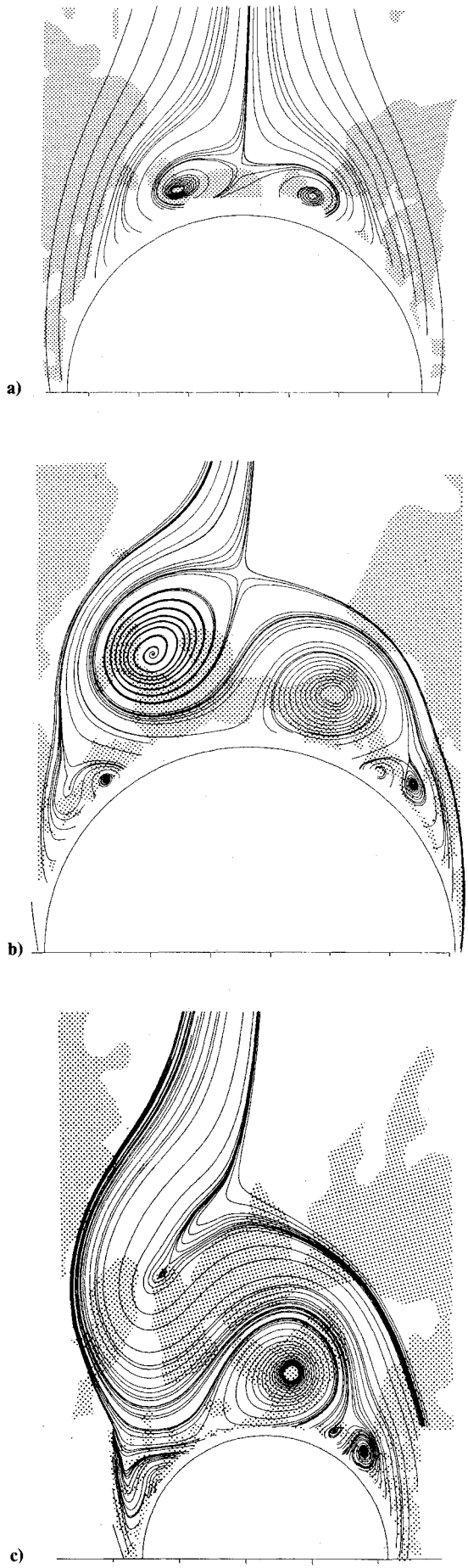

Fig. 7 Cross-flow plane streamlines determined by integrating Eq. (2) (shaded regions represent areas of negative $\partial u/\partial x$).

In one of the cases listed in Table 1, the strength of the secondary region S1 is marked with an asterisk. Here the surveyed portion of the flowfield clearly omits areas of high vorticity and the calculated strength is unreasonably low. These tabulated values are estimated using the known ratio of $\lambda_{s1\,\text{left}}$ to $\lambda_{s1\,\text{right}}$ from nearby cross-flow planes and the measured value of $\lambda_{s1\,\text{right}}$.

Asymmetric Development

Flowfield asymmetry was noticeable at all the surveyed cross-flow planes. At the two most forward stations probed, asymmetry is primarily associated with the primary saddle point region. At the foremost survey plane with $X/D=0.75$ (not shown), the outer edges of two primary vortices are visible. Here the primary saddle point is likely offset to the left. As in shown in Fig. 5a, two primary vortices are visible at $X/D=1.3$, but the secondary vortex structure is still not present. Although the two primary vortices appear to be symmetrically located, the rear attachment point (marked by S_a') is slightly offset to the right. Also, the velocities between the two vortices (second row behind the model) are all pointing to the left.

At an axial station of $X/D=2.6$, both primary and secondary vortices are visible in Fig. 5b. Here the entire vortex structure is clearly asymmetric. The left primary vortex has moved away from the model surface, while the right primary vortex has rotated toward the leeside. Two counterrotating secondary vortices are visible on each side of the model and these structures are relatively symmetrically disposed. The same flowfield structure persists at the axial station of $X/D=3.6$, but in this case the flowfield asymmetry is more extreme.

The maximum measured side force coefficient occurs at $X/D=4.7$ and the accompanying flowfield structure differs from that measured at $X/D=2.6$ and 3.6 In Fig, 5c only the right primary vortex is clearly visible. The secondary region has become highly skewed with the rear attachment points and secondary separation points rotated in a counterclockwise direction. On the right side of the model, two counterrotating secondary vortices are present, while on the left side only the secondary vortex rotating in a counterclockwise manner can be seen. An examination of the flowfield adjacent to the left primary separation point indicates the formation of a region of counterclockwise rotation. Although this is not particularly evident in Fig. 5c, the circulation of a number of adjacent elements in this region is positive, suggesting the formation of a new secondary vortex.

Circumferential pressure profiles measured at the axial stations of $X/D=2.6$, 3.6, and 4.7 are shown in Fig. 4. It can be seen that flowfield asymmetry produces differing levels of pressure on each side of the model. The lowest pressures occur on the side of the model with the closest primary vortex. The differing pressure levels present on each side of the model are bridged by sharp pressure gradients on the leeside of the model. These gradients extend from below each primary vortex core to the rear attachment point and are indicated by a G in Fig. 5. At an X/D of 2.6, both primary vortices are located fairly close to the model surface and two pressure gradients of opposite sign occur. At $X/D=4.7$, only the right primary vortex induces a sharp pressure gradient. Also indicated by a P in Fig. 5 are location where the pressure standard deviation reaches peak value. These peak values are located in the vicinity of the large pressure gradients and are likely caused by an unsteady circumferential motion of the vortex pattern. Such unsteadiness moves the position of the surface pressure gradients and produces large pressure fluctuations at nearby fixed points on the model.

A comparison of Figs. 4 and 5 indicates that secondary vortices have little discernable effect on the measured surface pressures. This is probably attributable to the small circulation strengths of these structures. Table 1 indicates that the circulation contained in th S2 region is typically small. The

strength of the vortex in S1 cannot be determined since this region contains both a strong shear layer and a vortex.

V. Cross-Flow Plane Topology

Construction and Interpretation of Cross-Flow Plane Streamlines

In the preceding section velocity measurements have been used to develop a qualitative description of the formation of flowfield asymmetry. An alternative description of this process can be given in terms of cross-flow plane streamlines that can be constructed from velocity measurements. The cross-flow plane streamline pattern provides a more quantitative definiton of the measured flowfield than can be gained simply by considering velocity data. Singular points, where the cross-flow plane velocity is zero, are clearly defined by the cross-flow plane streamline pattern. The location of these points as well as the streamline behavior throughout the cross-flow plane serve to sepecifically characterize the flowfield in a manner useful for comparing different sets of velocity measurements.

In interpreting cross-flow plane streamline patterns, it is important to note that cross-flow plane streamlines are not the projection of three-dimensional streamlines onto the cross-flow plane.[17,18] In particular, the cross-flow plane streamlines may exhibit a behavior not representative of three-dimensional streamlines. This is unfortunate since it means that the structure of the three-dimensional flowfield cannot be inferred from cross-flow plane streamlines. However, streamlines constructed on any plane will not accurately represent three-dimensional streamlines that must be constructed using three-dimensional data. In the absence of such information, which would be difficult to obtain, the cross-flow plane appears to be as satisfactory as any on which to construct plane streamlines.

Cross-flow plane streamlines can be generated by integrating the equations

$$\frac{dy}{dt} = v \qquad \frac{dz}{dt} = w \tag{2}$$

from a starting point. The starting points are selected by trial and error to highlight regions near vortices and separation points. To evaluate Eqs. (2), a description of v and w throughout the surveyed portion of the cross-flow plane is necessary. Such a description is constructed using a bilinear interpolation function of the form $a+by+cz+dyz$ to specify each velocity component within an element. Here a, b, c, and d are constants evaluated using the measured velocities at the corners of the element.

The cross-flow plane streamlines determined by integrating Eqs. (2) are shown in Fig. 7 for X/D stations of 1.3, 2.6, and 4.7 and exhibit several types of singularities. Saddles occur on the model surface as attachment or separation points. Also classed as saddles are cross-flow plane stagnation points interior to the flowfield that are formed by the intersection of four streamlines, two directed toward the singularity and two directed away from it. Focus singularities occur near the center of cross-flow plane vortices and are stagnation points about which the streamlines spiral or circle. Assuming that the cross-flow plane is a continuous vector field and that singularities are limited to points, it can be proved that the following relation must exist between the number of focuses and saddles[18]:

$$N_f - N_s - \tfrac{1}{2}(N_s') = -1 \tag{3}$$

where N_f is the number of focuses and N_s' and N_s represent the number of saddles on and off the body, respectively. This rule does not define cross-flow plane structure but precludes certain structures. It may also point to the existence of certain flowfield features that are not resolvable with experimental data.

In discussing cross-flow plane topology, focuses occuring in the primary and secondary vortices will be referred to as primary and secondary, respectively. The saddle or stagnation point occurring between the two primary vortices will be termed the primary saddle, as it was in the preceding section.

The cross-flow plane streamlines shown in Fig. 7 exhibit peculiarities that are probably not representative of three-dimensional streamline behavior. Cross-flow plane streamlines originating near the estimated primary and secondary separation points do not feed into vortices, but instead skirt the recirculatory regions. This behavior is unexpected, since three-dimensional streamlines originating near the separation lines can be expected to feed into the vortices. It is also questionable whether cross-flow plane streamlines near the focuses reflect three-dimensional streamline behavior. Here, the streamlines in the cross-flow plane are often observed to spiral outward from the focuses. The three-dimensional streamlines near the vortex core might be expected to spiral inward since, in general, the flow accelerates along the vortex core unless breakdown is imminent and breakdown is not anticipated in the vicinity of the surveyed flowfield.

As can be seen from examining Figs. 7a and 7b, between the axial stations of $X/D = 1.3$ and 2.6, the direction of the spiral of streamlines about the left primary focus changes. The intermediate streamline patterns between these two axial stations must exhibit a continuous transition between an inward and outward spiral. It has been suggested that spiral direction reversal may be accomplished by a limit cycle.[19] More complex patterns featuring multiple limit cycles are also possible, but the definition of the transitional sequence cannot be determined with certainty without additional experimental data. One possibility is the formation of a limit cycle near the outer edge of the region containing streamlines that spiral about the focus. Inside this limit cycle the streamlines spiral

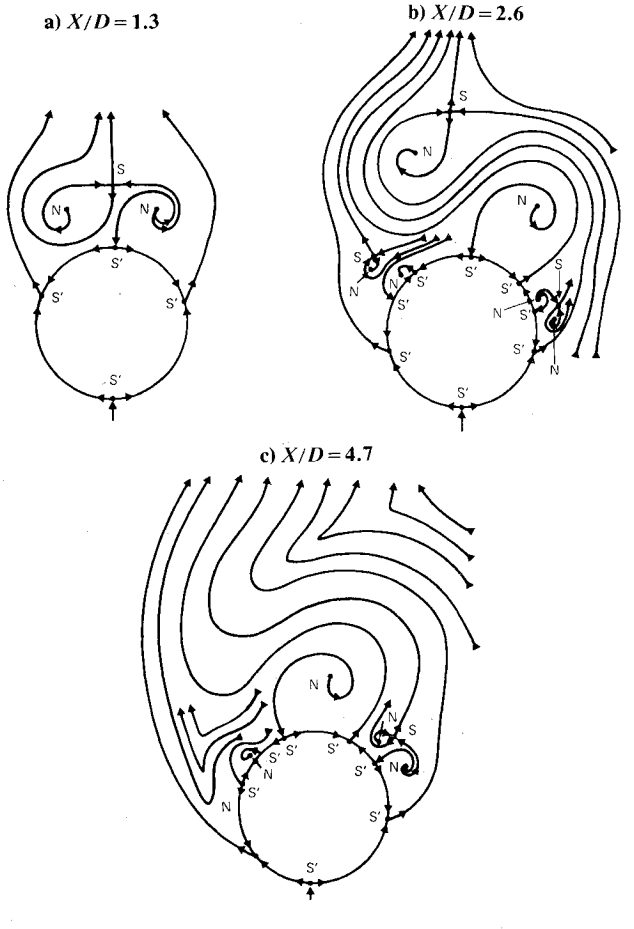

Fig. 8 Cross-flow plane topology.

outward, while outside of it they spiral inward. With increasing axial distance from the nose tip, the diameter of the limit cycle decreases and finally vanishes, leaving a focus with an inward spiral.

The parameter $\partial u/\partial x$ is very useful in interpreting the cross-flow plane streamline patterns.[19] By continuity, an inward vortex spiral implies $\partial u/\partial x > 0$ while an outward vortex spiral indicates $\partial u/\partial x < 0$. The distribution of $\partial u/\partial x$ throughout the flowfield can be determined by dividing the flowfield into quadrilateral elements with the corners located at the points where data were taken. Computing a mass balance for each element and applying continuity provides an estimate of the average value of $\partial u/\partial x$ for each element,

$$\frac{\overline{\partial u}}{\partial x} = \frac{1}{A}\oint \bar{V}\mathrm{d}\bar{s} = \frac{1}{2A}\left[\bar{n}_{12}\cdot(\bar{v}_1+\bar{v}_2)+\bar{n}_{23}\cdot(\bar{v}_2+\bar{v}_3)\right.$$

$$\left.+\bar{n}_{34}\cdot(\bar{v}_3+\bar{v}_4)+\bar{n}_{41}\cdot(\bar{v}_4+\bar{v}_1)\right] \quad (4)$$

where $\bar{n}_{ij}$ is the vector with magnitude equal to the distance between point i and j with the direction normal to the element edge and directed toward its center. The $\bar{v}_i$ quantity represents the velocity components at corner i and A is the element area. The resulting values of $\partial u/\partial x$ are assigned to the element's centroid location. Regions featuring negative $\partial u/\partial x$ values are illustrated by the shaded areas in Fig. 7. The reason for the alteration in direction of spiral of the left primary focus shown in Figs. 7a and 7b can be determined by examining the depicted regions of negative $\partial u/\partial x$. At $X/D=1.3$, the left primary focus is immersed in a region with negative $\partial u/\partial x$, while at $X/D=2.6$ this focus has moved into a region of positive $\partial u/\partial x$. A mass balance over the area near the focus containing spiraling streamlines indicates a change in the sign of $\partial u/\partial x$ average between these two axial stations.

Using the streamlines shown in Fig. 7 as a guide, sketches illustrating the topological structure of the surveyed cross-flow planes are shown in Fig. 8. In each sketch, the number of nodes and saddles satisfies Eq. (3). In Fig. 8c the left primary vortex and primary saddle are shown as combined. Inclusion of these two structures would also satisfy Eq. (3).

Flowfield Development

Using the streamline traces of Fig. 7 it is possible to construct a description of vortex shedding in terms of saddle and focus singularities. Small perturbations near the primary saddle point lead to a detachment of the windward streamline from the body surface. At the foremost survey station, which is shown in Fig. 7a, this streamline circles one focus and passes out the leeside of the flowfield. This topology is illustrated in Fig. 8a and features primary focuses that are still relatively symmetrically located and have a definite outward spiral. As the cross-flow plane asymmetry increases, the circled focus moves away from the model and reverses its direction of spiral to inward, as illustrated in Fig. 7b. The windward streamline from the primary saddle now feeds into this focus and the resulting cross-flow plane topology is depicted in Fig. 8b. A continuous transition between the topologies of Figs. 8a and 8b must occur. As discussed in the previous section, the reversal in focus spiral direction is likely accomplished by means of limit cycles. Further asymmetry development leads to a combination of the left primary focus and saddle. Figure 7c suggests that such a combination occurs, while Fig. 8c illustrates the resulting topology. Clearly, in order to satisfy Eq. (3), the left focus and primary saddle must simultaneously disappear from the flowfield. The combination of the primary saddle and the left primary focus provide a clear topological landmark in the asymmetry development process.

It has been suggested that flowfield asymmetry is a manifestation of a hydrodynamic instability that develops when primary vortices are crowded together.[20] Peake et al.[11] form the hypothesis, based on Nishioka and Sato's incompressible cylinder data,[21] that amplification of perturbations in the flowfield near the primary saddle point results in the development of the asymmetric flowfield. Irregularities in the model geometry serve only to determine the extent and direction of the flowfield asymmetries. The results from the current study support the hypothesis that the region near the primary saddle point plays a principal role in the formation of the asymmetric flowfield. The forwardmost cross-flow plane completely surveyed occurs at $X/D=1.3$. As shown in Figs. 5a and 7a here the focuses appear relatively symmetrially located. However, the windward streamline from the primary saddle point does not attach to the body surface, but instead circles about one of the primary focuses, as is indicated in Fig. 7a. Thus, it seems to be this streamline that first reflects flowfield asymmetry and, presumably, only small perturbations in the vicinity of the saddle point are sufficient to cause this streamline to detach from the model surface.

VI. Summary and Conclusions

A tangent ogive model with a nose fineness of 3 has been tested in incompressible flow at an incidence of 45 deg and with a Reynolds number producing laminar separation. The model was rigidly supported in the wind tunnel having a streamwise turbulence level of 0.1%. A grit trip was placed on the model to stabilize the flowfield. Both surface pressures and cross-flow velocities were measured on select cross-flow planes. A two-component LDV system was used to probe the flowfield near the primary separation points as well as further out from the model. Axial stations upstream of the location at which the maximum side force occurred were investigated. Based on the data taken in this study, the following conclusions can be drawn:

1) Use of a grit trip near the model nose stabilizes the flowfield without changing its basic side force characteristics.

2) In addition to two primary vortices, the flowfield generally contains two counterrotating secondary vortices on each side of the model.

3) Cross-flow plane streamlines have been constructed using experimentally measured cross-flow plane velocities. The cross-flow plane topology differs significantly from that expected to result from projecting three-dimensional streamlines onto the cross-flow plane.

4) In terms of the cross-flow plane topology, the development of the highly asymmetric flowfield up to the point of maximum side force can be characterized by the following three steps:

a) Flowfield asymmetries seem to originate with instabilities near the primary saddle point. The windward streamline leaving this point detaches itself from the body surface, circles about one of the primary focuses and then moves out into the leeward flowfield.

b) The focuses circled by this primary saddle point streamline moves away from the model and changes its direction of spiral.

c) The primary saddle and a primary focus appear to combine near the plane at which the peak side force occurs.

Acknowledgments

This project was supported by William C. Volz of the Naval Air Systems Command. The authors wish to thank Cmdr. Paul Schlein and his staff at the U.S. Naval Academy for making the wind-tunnel testing facilities available. D. Sternklar and C. Meseke also made significant contributions to this project.

References

[1] Gowens, F. E. and Perkins, E. W., "Study of the Effects of Body Shape on the Vortex Wakes of Inclined Bodies at $M=2$," NASA RM A53I17, 1953.

[2] Fiechter, M., "Uber Wirbelsysteme an Schlanken Rotationskorpern and Ihren Einfluss auf die Aerodynamischen Beiwerte,"

Deutsch-Franzosisches Forschungsinstitut, Saint-Louis, Bericht 10/66, 1966.

[3]Thomson, K. D. and Morrison, D. F., "The Spacing, Position and Strength of Vortices in the Wake of Slender Cylindrical Bodies at Large Incidence," *Journal of Fluid Mechanics*, Vol. 50, No. 4, 1971, pp. 751-783.

[4]Clark, W. H. and Nelson, R. C., "Body Vortex Formation on Missiles at High Angles of Attack," AIAA Paper 76-65, 1976.

[5]Clark, W. H.; "Body Vortex Formation on Missiles in Incompressible Flows," AIAA Paper 77-1154, 1977.

[6]Fidler, J. E., Schwind, R. G., and Nielsen, J. N., "Investigation of Slender-Body Vortices," *AIAA Journal*, Vol. 15, Dec. 1977, pp. 1736-1741.

[7]Yanta, W. J. and Wardlaw, A. B., "Laser Doppler Velocimeter Measurements of Leeward Flowfields on Slender Bodies at Large Angle-of-Attack," AIAA Paper 77-660, 1977.

[8]Schwind, R. G. and Mullen, J., "Laser Velocimeter Measurements of Slender Body Wake Vortices," AIAA Paper 79-0302, 1979.

[9]Owen, F. K and Johnson, D. A., "Wake Vortex Measurements of an Ogive Cylinder at $\alpha = 36$ Degrees," *Journal of Aircraft*, Vol. 16, Sept. 1979, pp. 577-583.

[10]Wardlaw, A. B. and Yanta, W. J., "The Flow Field about and Forces on Slender Bodies at High Incidence," AIAA Paper 80-0184, 1980.

[11]Peake, D. J., Owen, F. K., and Johnson, D. A., "Control of Forebody Vortex Orientation to Alleviate Side Forces," AIAA Paper 80-0183, 1980.

[12]Yanta, W. J. and Wardaw, A. B., "Multi-Stable Vortex Patterns on Slender, Circular Bodies at High Incidence," *AIAA Journal*, Vol. 20, April 1982, pp. 509-515.

[13]Lamont, P. J. and Hunt, B. L., "Pressure and Force Distributions on a Sharp-Nosed Circular Cylinder at Large Angles of Inclination to a Uniform Subsonic Stream," *Journal of Fluid Mechanics*, Vol. 76, No. 3, 1976, pp. 519-559.

[14]Wardlaw, A. B. and Morrison, A. M., "Induced Side Forces at High Angles of Attack," *Journal of Spacecraft and Rockets*, Vol. 13, Oct. 1976, pp. 589-593.

[15]Yanta, W. J. and Wardlaw, A. B., "An Experimental Study of the Primary and Secondary Separation Regions of a Slender Body at High Incidence," NSWC TR 82-394, Sept. 1982.

[16]Canning, T. N. and Nielson, J. N., "Experimental Study of the Influence of Supports on the Aerodynamic Loads of an Ogive Cylinder at High Angles of Attack," AIAA Paper 81-0007, 1981.

[17]Hunt, J.C.R., Abell, C. J., Peterka, J. A., and Woo, H., "Kinematical Studies of the Flows Around Free or Surface-Mounted Obstacles; Applying Topology to Flow Visualization," *Journal of Fluid Mechanics*, Vol. 86, No. 1, 1978, pp. 179-200.

[18]Tobak, M. and Peake, D. J., "Topology of Two-Dimensional and Three-Dimensional Flows," AIAA Paper 79-1480, 1979.

[19]Tobak, M., NASA Ames Research Center, Moffett Field, Calif., Private communication, Dec. 1982.

[20]Keener, E. R. and Chapman, G. T., "Similarities in Vortex Asymmetries over Slender Bodies and Wings," *AIAA Journal*, Vol. 15, Sept. 1977, pp. 1370-1372.

[21]Nishioka, M. and Sato, H., "Mechanism of the Determination of the Shedding Frequency of Vortices Behind a Cylinder at Low Reynolds Number," *Journal of Fluid Mechanics*, Vol. 89, No. 1, 1978, pp. 49-60.